

**Highly heterogeneous pore fluid pressure enabled rupture of orthogonal faults
during the 2019 Ridgecrest Mw7.0 earthquake**

Qibin Shi^{1,2}, Shengji Wei^{1,2}

¹Earth Observatory of Singapore, Nanyang Technological University, Singapore.

²Asian School of the Environment, Nanyang Technological University, Singapore.

Corresponding authors: Qibin Shi, (QSHI003@e.ntu.edu.sg); Shengji Wei (shjwei@ntu.edu.sg)

Key Points:

- The rupture process of the Ridgecrest Mw7.0 earthquake is represented by six subevents whose source parameters are constrained by local strong-motion data.
- Two subevents of the mainshock occurred on the SW-striking conjugate fault, while the major rupture propagated on the NW-striking fault system.
- Subevents and seismicity demonstrate the highly complex fault geometry, and the orthogonal fault coseismic rupture is most likely the result of high pore fluid pressure.

Abstract

Here, we show that the 2019 Mw7.0 Ridgecrest mainshock as well as its Mw6.5 foreshock ruptured orthogonal conjugate faults. We invert the waveforms recorded by the dense strong-motion network at relatively high frequencies (up to 1Hz for P, 0.25Hz for S) to derive multiple point source models for both events, aided by path calibrations from a Mw5.4 earthquake. We demonstrate that the mainshock started from a shallow (3 km) depth with a Mw5.2 event, and ruptured the main fault branches oriented in the NW-SE direction. At ~11 s, two Mw6.2 subevents took place on the SW-NE oriented fault branches that conjugate to the main fault to the NE and SW. The SW branch rupture partially overlapped with the foreshock rupture. We suggest the coseismic rupture on nearly orthogonal faults was enabled by high pore fluid pressure, which greatly weakened the immature fault system in a heterogeneous way.

Plain Language Summary

Earthquakes, which are caused by shear dislocation processes on faults, often rupture single faults or multiple faults oriented at acute angles. However, rupture of orthogonal faults (i.e., faults oriented at 90 degrees to each other) has until now been considered unfavourable based on the basic Mohr circle analysis. Here, we show that two large July 2019 earthquakes (Mw6.5 and Mw7.0) ruptured fault segments that are perpendicular to each other, with one NW-trending and the other SW-trending. We suggest that the complex fault slip is the result of a young fault system, aided by high heterogeneous pore fluid pressure.

1 Introduction

Imaging the rupture initiation and propagation of an earthquake provides critical information to understand its fundamental physics. However, gaining further insights into physical processes can be challenging, because earthquakes usually both start and develop in a fairly complicated manner. One such example is the 2019 Ridgecrest earthquake sequence, which ruptured un-mapped fault segments within the Eastern California Shear Zone (ECSZ) between the Garlock fault and the Wilson Canyon fault (Figure 1a inset, Figure S1). The earthquake sequence produced very complex surfaced ruptures [Brandenberg *et al.*, 2019] and numerous aftershocks on tens of fault segments [Ross *et al.*, 2019; Shelly, 2020]. Surface deformation was very well recorded by geodetic observations including GPS and satellite images

[Fielding *et al.*, 2020; Floyd *et al.*, 2020; Mattioli *et al.*, 2020; Melgar *et al.*, 2019; K Wang and Bürgmann, 2020; X Xu *et al.*, 2020]. All these observations have clearly shown that the sequence ruptured conjugate faults. In addition, foreshock seismicity [Ross *et al.*, 2019; Shelly, 2020] and rupture process studies [Feng *et al.*, 2020; Liu *et al.*, 2019] indicate that conjugate fault segments ruptured during the Mw6.5 foreshock. As for the mainshock coseismic rupture processes, so far only the main fault segments, oriented in near NW-SE direction, have been investigated [Barnhart *et al.*, 2019; Bilham and Castillo, 2020; Chen *et al.*, 2020; Feng *et al.*, 2020; Goldberg *et al.*, 2020; Li *et al.*, 2020; Liu *et al.*, 2019; Lozos and Harris, 2020; Qiu *et al.*, 2020; Yang *et al.*, 2020; Zhang *et al.*, 2020], and it is not clear whether the SW-oriented conjugate fault segments ruptured as well. It is difficult to use InSAR/SAR data to resolve the mainshock coseismic rupture on the conjugate fault (SW-NE oriented), because the mainshock occurred only ~34 hours after the foreshock, and most geodetic observations (i.e. InSAR, SAR) have recorded surface deformation from both events. The high-rate and static GPS observations have a better temporal resolution, but are too sparse to provide a sufficient spatial resolution [Melgar *et al.*, 2019]. The local strong-motion network, on the other hand, has a much better spatial and temporal coverage (Figure S1). This network provides a unique dataset to resolve the coseismic rupture process of the largest event in the sequence, including the initiation and propagation of the rupture. Compared with finite fault models (FFM) [Hartzell and Heaton, 1983; Kikuchi and Kanamori, 1982; Wei *et al.*, 2013a; Yoshida *et al.*, 1996], the multiple point source (MPS) inversion approach we use [Shi *et al.*, 2018] does not assume a specific fault geometry, and focuses more on first-order complexity of the rupture. Furthermore, MPS inversion requires much fewer parameters than FFM, and is therefore much less prone to data over-fitting. The robustness of MPS inversion was confirmed by a path calibration technique which has been demonstrated as very powerful [Shi *et al.*, 2018; Wei *et al.*, 2013b; Wei *et al.*, 2018; Wei *et al.*, 2015]. The abundant aftershocks of the 2019 Ridgecrest sequence allow us to select an appropriate calibration event to identify the most reliable paths and components for inversion, and invert waveforms of the target event at much higher frequencies.

Another issue that has not yet been well addressed is the initial rupture of the mainshock. Various hypocenter estimations have been suggested. The Southern California Earthquake Data Center (SCEDC) reported a hypocenter depth of 8.0 km, which is used by most kinematic rupture models of the event (e.g., Liu *et al.* [2019]). Meanwhile, Ross *et al.* [2019] reported an

extremely shallow hypocenter depth of 1.0 km, and *Lomax* [2020] reported a hypocenter of 4.2 km. The recordings of the CLC strong-motion station (Figure 1a), only 5.2 km away from the mainshock hypocenter, along with other nearby stations allow us to further refine the initial rupture process of the earthquake, thus providing critical observations to understand the implication of the initial rupture for this very complicated event.

In this study, we start from introducing the MPS inversion and waveform analysis of the calibration event. We then show the MPS inversion results for the mainshock and foreshock, along with the modeling of the beginning waveform recorded by the CLC station for the initial rupture of the mainshock. We then discuss the implication of our MPS models and the mainshock dynamic triggering and initiation.

2 Multiple Point Source Inversion Strategy and Path Calibration

To study the rupture processes of the Mw7.0 mainshock and the Mw6.5 foreshock, we download the strong-motion waveform data from Southern California Earthquake Data Center [SCEDC, 2013] and Center for Engineering Strong Motion Data. We select the stations within 20 km for both earthquakes (Figure S1). Waveforms on farther stations is not used as they are too complicated to be modeled at the frequency that is meaningful for resolving the detailed rupture. We carefully handpick the first P-wave arrivals, which are used to align data and synthetics in the inversion. Interestingly, for the mainshock we identify a weak pulse arriving a few seconds (< 2 s) before the strong P-wave onsets on the 14 closest stations (Figure 3c), which is also captured by *Lomax* [2020]. We later relocate the mainshock hypocentre and the source of the weak pulse (next section).

For MPS inversion using the strong-motion data, we apply the Markov-Chain-Monte-Carlo (MCMC) sampling algorithm proposed by *Shi et al.* [2018], conducted in an iterative fashion. We start the inversion using two point-sources and gradually increase the number of sources until no dramatic reduction in misfit. We run the inversions with little prior information, only using the earthquake magnitude and rupture area to constrain the searching ranges of the parameters.

As demonstrated in previous analyses [*Shi et al.*, 2018; *Wei et al.*, 2013b; *Wei et al.*, 2018; *Wei et al.*, 2015], path calibration from a smaller event in the source region is critical for robust rupture process inversion. A good calibration event would allow us to determine the

frequency range and the components that should be used for the large events. We identify a Mw5.4 event (reported by SCEDC at 2019/07/05/11:07:53, 35.761°N/117.570°W/8.0km) near the mainshock hypocenter as a calibration event, as it is small enough to be considered as a point source at the frequency range we use, but also big enough to be well recorded by all the nearby strong-motion stations. We conduct calibration by point-source waveform inversion on the Mw5.4 event using the Cut-and-Paste method [Zhao and Helmberger, 1994; Zhu and Helmberger, 1996], which cuts three-component waveform at each station into P and S wave segments and fit them with different time shifts. Because path and site conditions vary among stations, we apply different filtering frequencies to P and S waves on different stations. The 1D SoCal model [Kanamori and Hadley, 1975] is used to compute the Green's functions by the FK method [Zhu and Rivera, 2002], which are also used later in the MPS inversions. The waveform cross-correlation between data and synthetics is very efficient and straightforward to eliminate the complicated paths that cannot be modelled by the synthetics. As this process is frequency dependent, here we push the frequency range as high as possible, while keeping the number of stations at a decent number (tens of stations). Furthermore, we discard some stations that are very close to other stations, to avoid the coverage of the stations being dominated in certain azimuthal range. This finally picks out 55 stations for the MPS inversions (see Table S2 for frequency ranges). The focal mechanism and waveform fits of the calibration event are shown in Figure S3. The P and S time shifts derived from the calibration waveform fitting are later utilized to correct the travel time in the MPS inversions of the large events. Through this way, we validate the reliability of the Green's functions at the selected frequency ranges.

3 Inversion and modeling results

We first present the inversion result for the foreshock (see Figure S2 for the statistics of the cross-correlation coefficients, Figure S4 for the waveform fits and Figure S5 for the uncertainties of parameters) and then the mainshock (see Figure S2 for the statistics of the cross-correlation coefficients, Figure S6 for the waveform fits and Figure S7 for the presentation of uncertainties from the MCMC inversion), followed by the hypocenter relocation and modeling of CLC station waveform for the mainshock.

Our inversion result shows that the Mw6.5 foreshock is well represented by three point-sources (Figure 2). The first subevent (F1, Mw6.12) is located near the hypocenter, at the depth

of 11 km. The seismicity of the foreshock sequence [Shelly, 2020] shows a NW-SE lineation that is consistent with one of fault plane solutions (strike=315°/dip=82°) of F1 (Figure 2a), we therefore considered it as the ruptured fault. The following subevents, F2 (Mw6.12) with centroid time at 6s and F3 (Mw6.16) with centroid time at 9s, however, are most likely located on the conjugated SW-NE oriented fault, as one of the fault plane solutions of F2 and F3 (strike=225-228°/dip=84-89°) is in remarkable agreement with the lineation of the seismicity. Note that F2 (6 km) and F3 (4 km) are much shallower than F1 (11 km). All three subevents have similar moment and source duration, approximately aligning in NE-SW direction and showing rupture directivity toward SW. The rupture directivity is clearly shown in the waveforms from different azimuths (Figure 2b). The LRL station (azimuth=213°), located towards the rupture direction, shows a single-pulse waveform, in contrast with CLC (azimuth=326°) station, located away from the rupture, showing clear three pulses in the waveform. The waveform decompositions at nearby stations present different sensitivities to the rupture process. For instance, F3 makes the largest contribution to almost all stations due to its slightly larger moment, except for MPM (azimuth=2°) where F1 makes the largest contribution, as F1 is closest to MPM. The robustness of the result is later discussed with the mainshock analysis.

By gradually increasing the number of subevents, we find that six sources are required to adequately model the mainshock waveforms. In Figure 1, the results of six subevents (M1-6) are plotted with the relocated aftershocks Shelly [2020], along with representative seismicity profiles (Figure 1b, A-D). The map view of the first subevent M1 (Mw6.38) is located ~3km to the southeast of the intersection of the surface ruptures and the seismicity near the epicenter, where the sub-vertical faults reverse their dipping direction from SW to the north to NE to the south [Ross *et al.*, 2019; X Wang and Zhan, 2020]. The NW-SE striking fault plane solution of M1 is dipping to NE, consistent with the fault geometry reconciling surface rupture and underground seismicity. M1 is a long duration sub-event (~10 s) compared with the other subevents, in particular M2 (Mw6.75) that is located 7 km to the NE of M1 and has the largest moment but only 7 s duration. The following rupture, represented by M3 (Mw6.45), is located slightly to the SW of M1, started at 7s and centroid at 10 s (duration 6s). M3 represents a near-vertical right-lateral fault segment, indicating the rupture of different fault branch compared with M1. This is

165 matching the double surface rupture traces near M1 and M3. Note the first three subevents
166 release ~74% of the total moment, dominating the radiated seismic energy. The next two
167 subevents (M4 and M5), which have almost the same moment ($M_w 6.26$ and $M_w 6.19$) and
168 centroid time (~14 s), are located to the SE and south of M3, respectively. Careful inspection of
169 the seismicity around M4, both in map view and vertical profile (Figure 1b), reveals that
170 aftershocks clearly align in NE-SW direction, conjugating to the main seismicity lineation and
171 surface rupture. The NE-SW oriented fault plane solution of M4 has a strike of 58° that is well
172 consistent with the seismicity lineation. We therefore consider M4 is located on the conjugate
173 fault rather than on the NW-SE trending main fault. Note that, although M4 is very close to F1 in
174 horizontal location, its depth is much shallower (3 km vs 11 km). The lineation of the seismicity
175 (Figure 1b, B) indicates that M4 probably took place on a fault that is parallel with the fault
176 segment ruptured in F2 and F3, instead of on the same fault of F1. M5 is another subevent that
177 we consider to be located on the conjugate fault that already ruptured during the foreshock. It is
178 located only 2 km to the west of F3 and slightly deeper (5 km vs 4 km), where seismicity lineated
179 in SW-NE direction. Interestingly, the M5 fault plane solution striking in SW-NE direction has a
180 dip angle of 60° , ~20° shallower than F3. The seismicity lineation in the depth profile (Figure
181 1b, A) also shows a shallower dipping fault geometry at depth greater than 5 km, remarkably
182 agrees with dip angle of M5. At about 16 s, the last subevent M6 ($M_w 6.35$) took place on the
183 southern portion of the NW-SE striking main fault, possibly involved with two parallel branches
184 of right-lateral strike-slip faults as shown in the surface rupture, although we cannot distinguish
185 them in our subevent solution.

186 To better understand the robustness of the six-point-source solution, in particular to the
187 subevent on the conjugate faults (i.e., M4 and M5), we decompose the synthetics into the
188 contribution from each subevent (Figure 3a) at the representative stations. Because the
189 mainshock is much larger in dimension compared with the foreshock, these nearby stations show
190 stronger variation of sensitivities to different parts of the rupture. In general, they are dominated
191 by the rupture closest to them, which is not necessarily the largest subevent (as highlighted by
192 circles in Figure 3a). For example, the down-going pulse of the N-S displacement component of
193 the CLC station is primarily from M1, and later on from M3. In contrast, the largest subevent M2
194 only generated weak N-S component as it sampled the nodal direction of SH radiation of M2.

Similarly, the E-W component of LRL station is clearly contributed more from M3, M4, and M6, rather than M2. The conjugate fault rupture M5 is clearly evidenced on the E-W component at the 5419 station (Figure 3a), which is closest to the subevent. If we force the inversion to exclude the rupture on this conjugate fault, the waveform fits to this component is dramatically reduced (94% vs 86% Figure 3b). Similar situation happens to LRL, a station to the south that is closer to M4 and M5 than other subevents. The statistics of waveform cross-correlation coefficients (Figure S2) also shows that the solution including the conjugate fault rupture indeed systematically fits the data better.

The robustness of the solution is further verified in waveform comparisons between the calibration event, foreshock and the mainshock (Figure 4). The calibration event records at all representative stations show simple, single-pulse waveform, and can be very well fitted by the 1D synthetics up to 1 Hz for P and 0.25 Hz for S waves (Figure S3). Similar degrees of fitting are obtained for the larger events, which show various complexities among stations. For instance, at LRL station, the foreshock waveform is simple (see previous text as well) but the mainshock waveform is very complex. But the situation reverses at CLC station that is located to the NE of the rupture zone. To simultaneously fit 50+ calibrated stations well actually places very strong constraints to the subevent solutions, in particular considering their much fewer parameters compared with finite fault models. This is further strengthened in the synthetic test (Figure S8).

The MPS solution, however, cannot explain the signals preceding the large P-wave onset identified at 14 stations (blue dots in Figure 3c), simply because they are too weak (Figure 3d). We term this source as a precursory event of the mainshock. The azimuth-dependent relative arrival times between the precursory event and the P-wave onset indicate a different location of the precursor. Using these arrival times, we relocated the precursor to $\text{lat}=117.564^\circ\text{W}$, $\text{lon}=35.746^\circ\text{N}$ and $\text{depth}=5\text{ km}$ (green star in Figure 1a) relative to the calibration event (see Figure S9a-c for more details). Based on the P-wave amplitude comparison with other nearby small events, we estimate the magnitude of the precursor to be $M_b\ 2.5$. Noted that the precursory event is located $\sim 5\text{ km}$ to the SE of the epicenter at a depth of 5 km and occurred 0.8s earlier. We also relocate the P-wave onset ($35.769^\circ\text{N}/117.593^\circ\text{W}/3\text{km}$, Figure S9d-f) relative to the calibration event, which is marked as red star in Figure 1a. This epicenter location is similar to the most, if not all, of the mainshock epicenter reports (e.g., SCEDC; Lin [2020]; Ross *et al.*

[2019]), but our depth is quite shallow (3 km). Moreover, to model the very beginning part of the CLC station waveform (Figure 3e and Figure S10) after the P-wave onset, we need a Mw5.2 event at the hypocenter, which is considered as the initial major rupture of the mainshock (P-wave onset).

4 Discussion and Conclusions

4.1 Interpretation of orthogonal fault ruptures

The two subevents (M5 and F3) on the conjugate fault are very close in space (Figure 5). For this conjugate fault segment, we do not see clear asperity separation in the published slip models (e.g., *Liu et al.* [2019]; *Li et al.* [2020]). The seismicity (profile A in Figure 1b) associated with M5 and F3 also highly overlaps. Hence, we suggest the mainshock (M5) re-ruptured a portion of the fault that had ruptured in the foreshock (F3), similar to the October 2016 Mw6.5 earthquake sequence in central Italy [*Ferrario and Livio*, 2018]. This repeated rupture implies that the foreshock released only a portion of the stress accumulated on the fault, with strong dynamic triggering during the mainshock (Figure 5). Thus although the conjugate fault had just ruptured during the foreshock, the fault must have been quite sensitive to stress perturbation caused by the mainshock, implying a weak fault. The maximum principle stress axis (σ_1 , compressional) from earthquake focal mechanism [*X Wang and Zhan*, 2020] and GPS data [*Savage et al.*, 2001] is oriented practically in the N-S direction (Figure 5). The angles between σ_1 and the left-lateral main fault and the conjugate fault are both $\sim 45^\circ$. Based on Mohr-Coulomb rupture criteria, this angle would require a very small friction coefficient (weak faults) (e.g., *Meng et al.* [2012]). On the other hand, slow rupture speed, high aftershock productivity [*Liu et al.*, 2019], and very complex fault geometry [*X Wang and Zhan*, 2020] all indicate an immature fault system, implying rougher and stronger faults in comparison with the neighboring plate boundary type fault (SAF). Recent rock experiments also show that conjugate fault ruptures tend to occur in rock samples with rougher fault friction [*Renard et al.*, 2020]. In addition, near-fault plastic deformation and encountering of rupture barriers [*S Xu and Ben-Zion*, 2013] were invoked to explain conjugate fault seismicity very close to the main rupture [*Ross et al.*, 2019]. This explanation requires strong heterogeneous stress or friction on the fault. To reconcile various observations and the friction contrast from different mechanisms of the sequence, we suggest that high pore fluid pressure played a key role in highly heterogeneous effective normal

stress on the fault. This high pore fluid pressure effect was likely very strong at least on the conjugate fault that ruptured in both the foreshock and mainshock. The immature fault system could have led to highly heterogeneous permeability on the fault, and hence to the highly variant effect of pore fluid pressure. This mechanism could be generalized to explain conjugate fault ruptures reported for several other events [Hudnut *et al.*, 1989; Meng *et al.*, 2012; Ruppert *et al.*, 2018; Scognamiglio *et al.*, 2018; Wei *et al.*, 2013a], which all took place on faults that are much less mature than the plate boundary type of faults.

The barrier mechanism proposed by *S Xu and Ben-Zion* [2013] cannot be used to explain M5, as M5 occurred too far away from the main fault branch to have been affected by plastic deformation. Instead, M5 could have been triggered by the dynamic shear wave field from M2, the largest subevent in the sequence. If we assume a shear speed of 3.0 km/s, the times of M5 and M6 ruptures are roughly consistent with M2 shear wave arrival time (wavy lines in Figure 5). The occurrence of M4, which ruptured the NE extended conjugate fault relative to the main fault, cannot be explained by *S Xu and Ben-Zion* [2013] mechanism either. Because M4 occurred in the compressional stress quadrant produced by the dynamic and static stress from preceding subevents. The reverse-fault slip component of M4 highlights the importance of incorporating both anti- and in-plane motions and of using a more realistic fault geometry in the dynamic simulations.

4.2 The mainshock rupture initiation and complex fault geometry

The initial rupture (Mw5.2) of the mainshock occurred 0.8 s after and ~5 km to the northeast of a precursor event (M_b2.5) (green stars in Figure 5). If preslip nucleation is used to explain these two sub-events, the nucleation size is at least 5 km, which is too large compared with that from dynamic simulations (e.g., *Lapusta and Rice* [2003]). The distance and timing difference between the two events also exclude the possibility that the Mw5.2 event was triggered by the S-wave from the M_b2.5 event. Instead, the mainshock was preceded by multiple shallow seismicity events near the location of the M_b2.5 event (Figure 2). We therefore suggest

the $M_b 2.5$ event was more likely an independent earthquake, unrelated to the nucleation of the mainshock.

The initial rupture ($M_w 5.2$) of the mainshock was very shallow, which is less common compared with other large events that start from the lower bound of the seismogenic zone, as stress concentration is more pronounced at the depth of brittle to ductile transition. The very shallow initial rupture of the Ridgecrest minshock was likely facilitated by stress perturbation from the foreshock (e.g., *Qiu et al.* [2020]). Note that this is in contrast with F1 (first subevent of the foreshock), which was deep (11 km), and probably located at the lower bound of the seismogenic zone defined by historical seismicity, or even slightly deeper [*Bonner et al.*, 2003]. In single fault plane dynamic rupture simulations, a shallower hypocenter depth corresponds to a rather large Ru number and small nucleation size h^* [*Barbot*, 2019; *Shi et al.*, 2020], and hence the entire fault is prone to rupturing during a large earthquake. However, our results show that the geometric complexity and the stress and friction status of the entire fault system, as well as dynamic triggering played important roles in shaping the size of the earthquake, which clearly poses additional challenges to the dynamic simulations of both single earthquakes and earthquake cycles.

The mismatch between seismicity and surface rupture traces indicates that a very complicated fault geometry was involved in the rupture. Seismicity shows many more conjugate fault branches than we can resolve with MPS inversion. We cannot exclude coseismic rupture on other conjugate fault segments. These features could be resolved with a higher-frequency waveform analysis. One possible way of pushing the limit of frequency ranges is back-projection of high-frequency radiators. However, as demonstrated by *Zeng et al.* [2020], careful error analysis, especially testing 3D source-side velocity structures, would be needed.

4.3 Summary

The orthogonal rupture and re-rupture of the SW conjugate fault segment revealed by MPS solutions for both the mainshock and foreshock requires weak faults in an immature fault system, suggesting heterogeneously distributed pore fluid pressure. Weak faults resulting from

heterogeneously distributed pore fluid pressure could explain other conjugate rupture earthquakes.

Acknowledgments

Strong-motion waveform data was downloaded from Southern California Earthquake Data Center using STP (<https://scedc.caltech.edu/research-tools/stp/>) and Center for Engineering Strong Motion Data (<https://www.strongmotioncenter.org>). We appreciate Dr. Chengli Liu for providing the baseline-corrected displacement waveform for comparison. Relocated seismicity data is available from *Shelly* [2020]. Figures were made with GMT-4.5.14 [*Wessel et al.*, 2013] and MATLAB. Seismic Analysis Code (SAC) was used extensively in this analysis. This work was supported by the Earth Observatory of Singapore research grant (XXX).

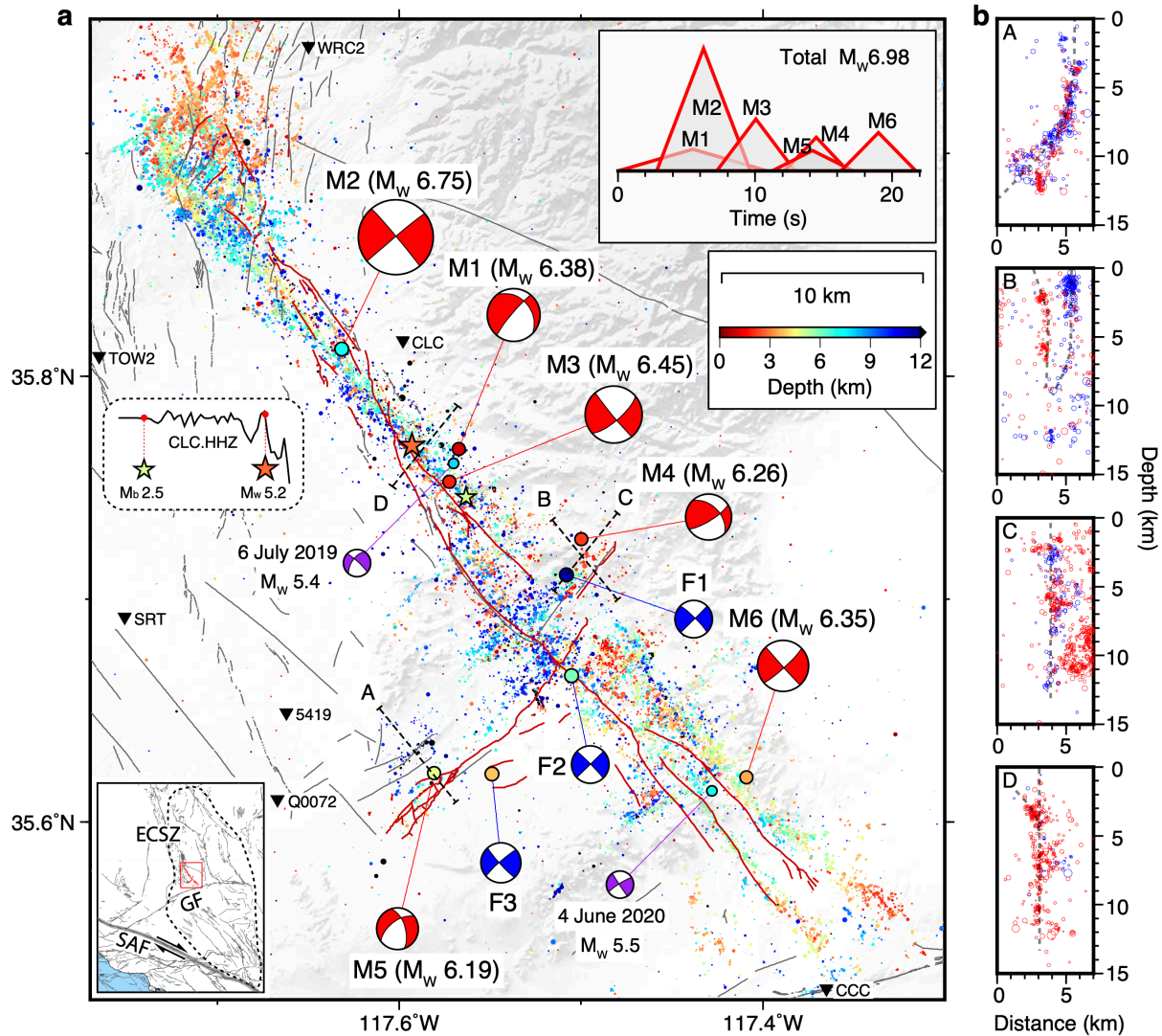


Figure 1. The Mw7.0 Ridgecrest mainshock MPS inversion result and aftershocks. (a) A map view of the mainshock subevents M1~6 and aftershock seismicity. Subevent focal mechanisms are the red beachballs with sizes proportional to moment magnitudes, connected with circles representing their centroid locations (color coded by depth). Two precursory events (stars) are illustrated in the dashed box. Aftershocks [Shelly, 2020] are the dots colored by depths and scaled with magnitudes. Surface ruptures [Brandenberg *et al.*, 2019] and previously mapped faults are plotted with red and gray lines, respectively. The triangles mark the nearest stations. The upper-right inset shows the source time function of each subevent, with areas proportional to their moments. The lower-left inset shows the earthquake region within the Eastern California Shear Zone (ECSZ), the San Andreas Fault (SAF) and the Garlock Fault (GF). The blue beachballs are the Mw6.5 foreshock subevents. The purple beachballs are Mw5+ events. (b) Seismicity projected to profiles A~D (shown in (a)). The red circles are aftershocks of the mainshock along profiles (within 1 km), while the blue circles are aftershocks of the Mw6.5 foreshock that happened before the mainshock (Figure 2a). The circle sizes are proportional to the events' magnitudes.

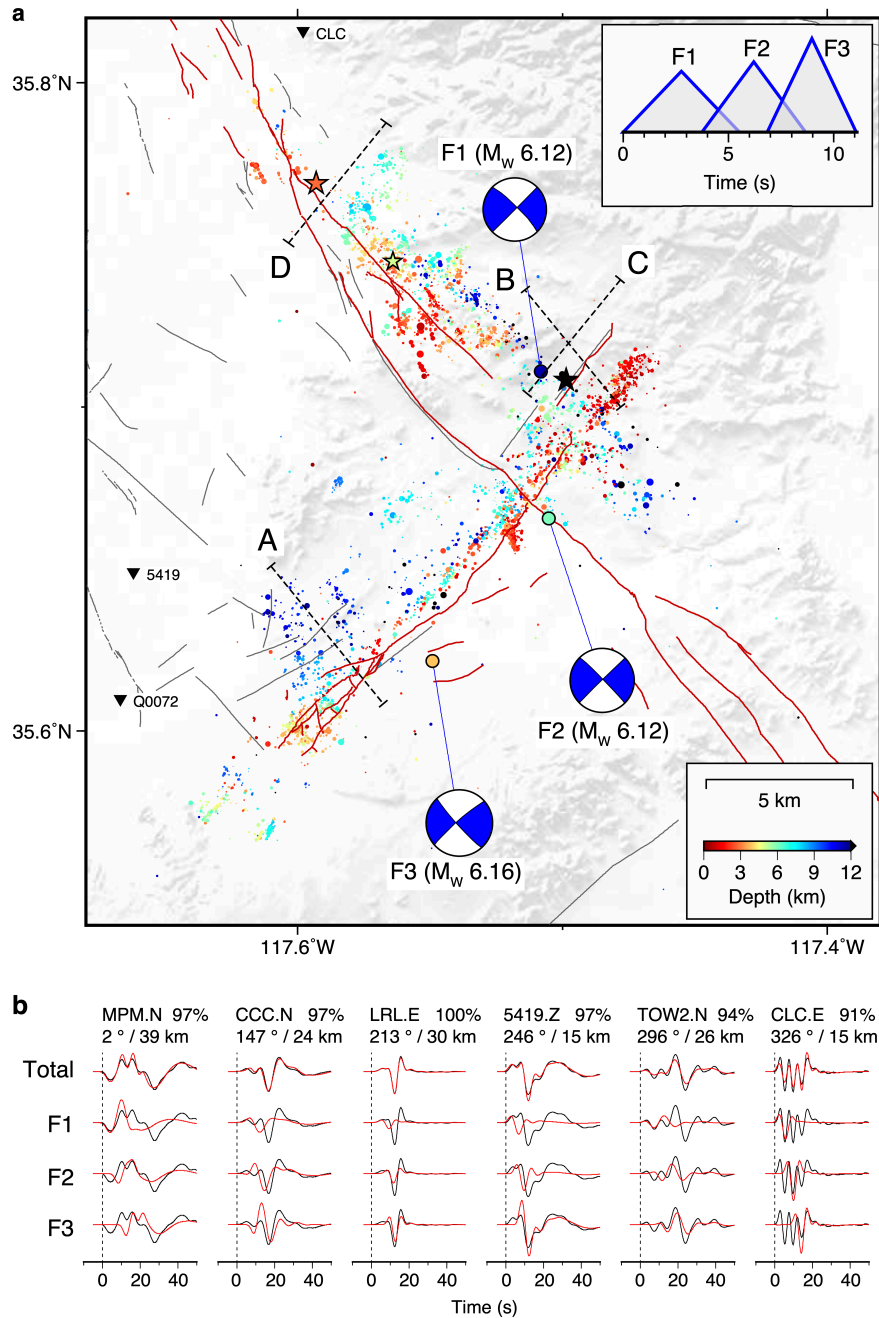


Figure 2. The Mw6.5 foreshock inversion results. (a) A map view of the Mw6.5 foreshock subevents F1~3 and seismicity [Shelly, 2020] before the mainshock (dots colored based on depth). Subevent focal mechanisms (beachballs), centroid locations (circles colored by depth), and source time functions (upper-right inset) are shown in the same way as in Figure 1a. Hypocenters of the foreshock (10 km) is the black stars. Mainshock precursors are green and orange stars. (b) Comparison between the synthetics computed with all subevents (red, Row 1) and the strong-motion observations (black) from six representative stations, along with the contribution from each subevent (red, Row 2-4), filtered to the same frequency ranges as in Figure 3a.

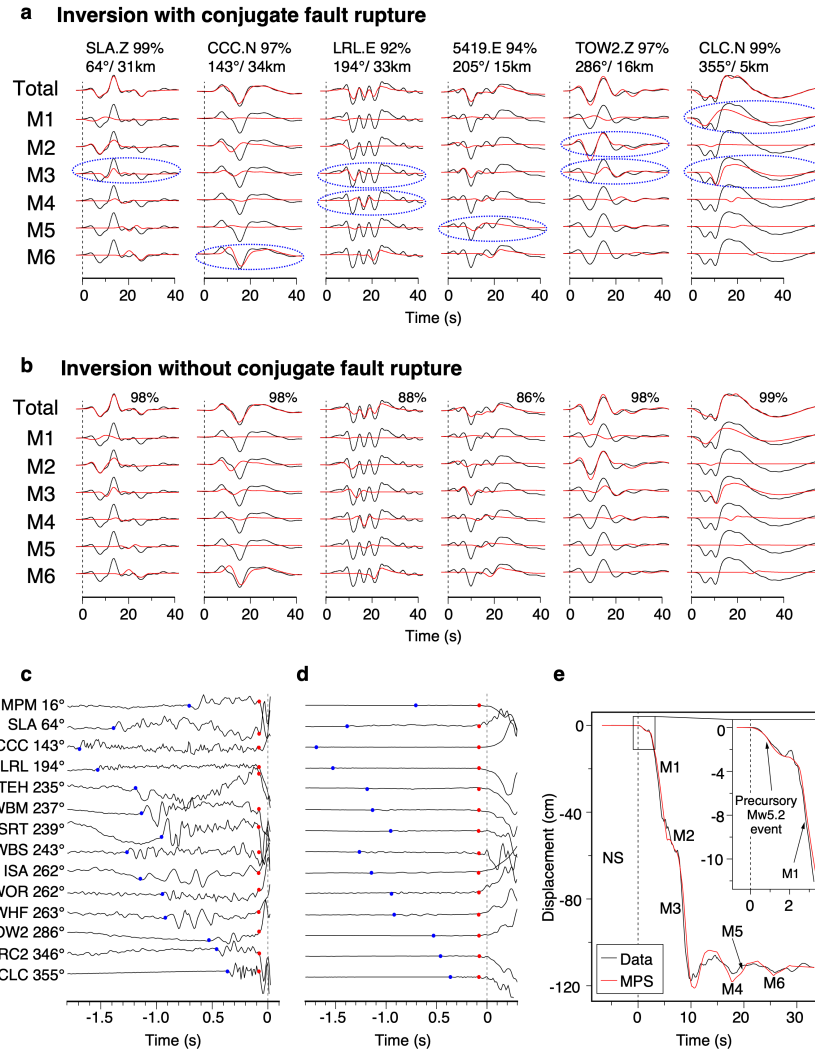


Figure 3. Interpretation of the mainshock strong-motion waveforms. (a) Comparison between the full synthetics computed with all six subevents (red, Row 1) and the strong-motion waveforms (black) recorded by six nearby stations, along with the contribution from each subevent (red, Rows 2–7 for M1–6), filtered to the frequency ranges used for inversions (Table S2). Station codes, waveform cross-correlation coefficients, station azimuths, and epicentral distances are denoted above the waveforms. (b) A controlled experiment of MPS inversion without rupture on the SW-oriented conjugate fault. The waveform comparison and cross-correlation coefficient are presented in the same way as in (a). (c) Handpicks of 14 stations closest to the Mb2.5 (blue dots), Mb3 (red dots), and Mw5.2 precursory events (dashed line) within 2 s before the mainshock P arrivals (0 s). Velocity waveforms are vertically normalized with the maximum amplitudes. (d) A larger time window that includes the mainshock P wave and its three precursory events, with the same handpicks as in (c). (e) Modeling the broadband displacement waveform of the CLC station with a Mw5.2 precursory event and the six subevents. The source durations or moment magnitudes of subevents are fine-tuned to better fit the waveform.

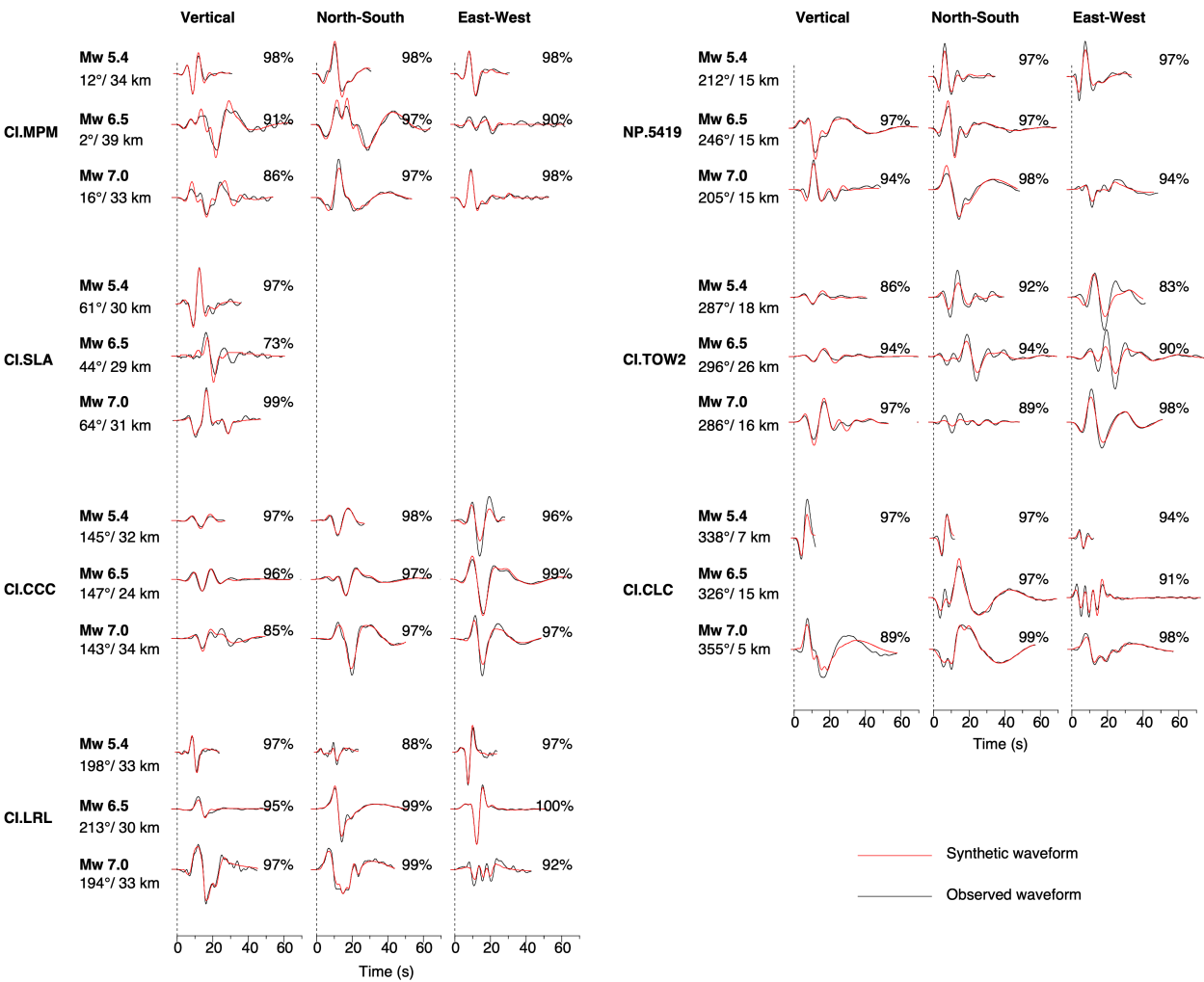


Figure 4. Comparison of synthetic and observed waveform fitting of the Mw5.4, Mw6.5, and Mw7.0 earthquakes. Vertical, NS, and EW components are scaled proportionally to reach the same maximum amplitudes for all station-event pairs. Station codes, azimuths, and distances are on the left, while cross-correlation coefficients are on the right of each component.

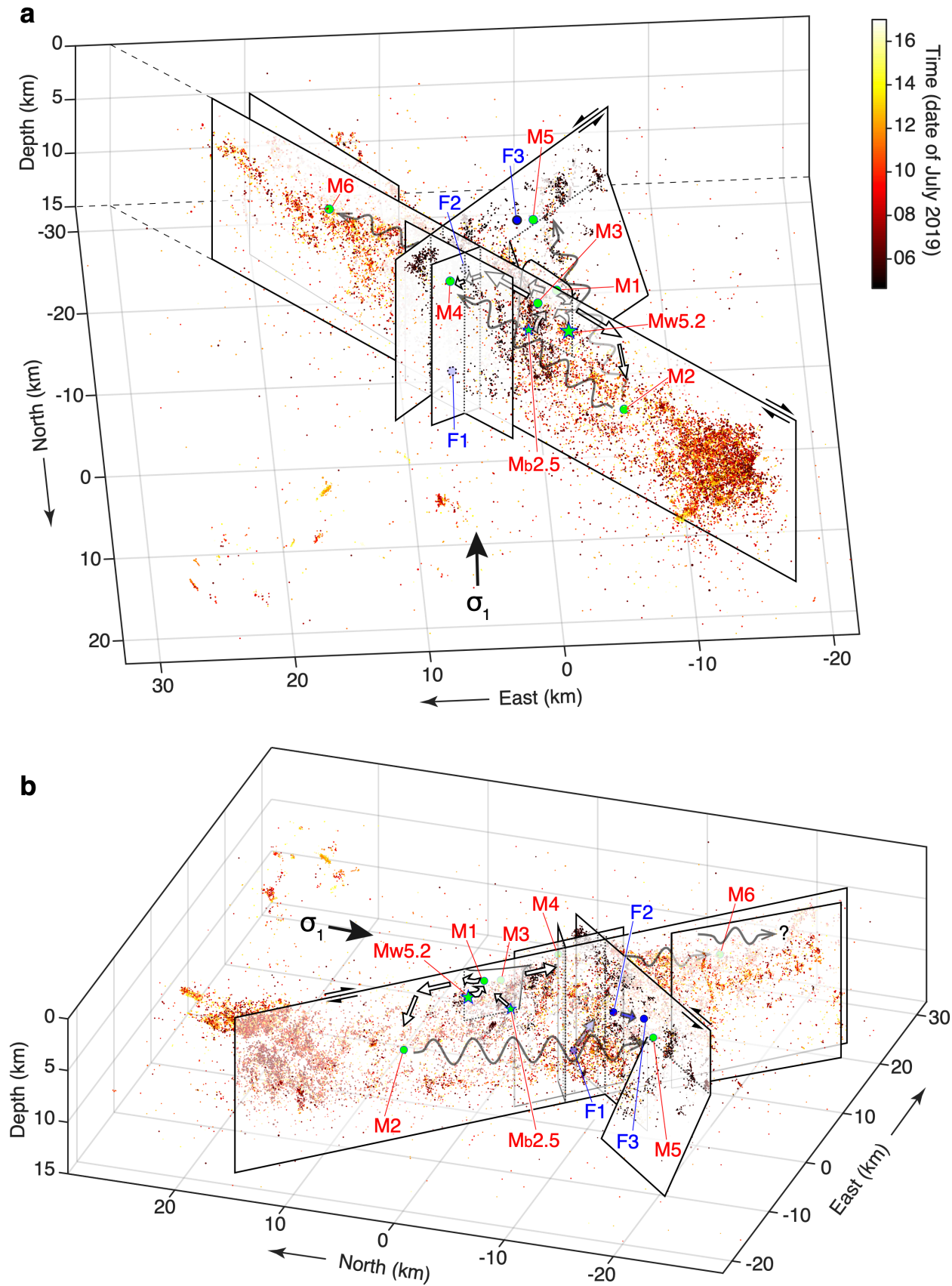


Figure 5. Schematics of the coseismic rupture initiation and propagation. (a) and (b) are from N and SW perspectives. Seismicity [Shelly, 2020] between 4 and 16 July 2019 is colored based on the day of occurrence. The precursory events (stars) near the intersections of the NE-dipping and the vertical faults precede the large mainshock subevents M1~6 (centroid locations denoted by the green circles) at different fault branches. The white arrows show the rupture propagation direction, while the gray wavy arrows indicate that the shear waves of M1–3, which triggered M4–6. The Mw6.5 foreshock subevents (blue circles) propagated from the deep to the shallow portions (blue arrows) of the two conjugate faults.

References

- Barbot, S. (2019), Slow-slip, slow earthquakes, period-two cycles, full and partial ruptures, and deterministic chaos in a single asperity fault, *Tectonophysics*, 768, 228171.
- Barnhart, W. D., G. P. Hayes, and R. D. Gold (2019), The July 2019 Ridgecrest, California, Earthquake Sequence: Kinematics of Slip and Stressing in Cross-Fault Ruptures, *Geophysical Research Letters*, 46(21), 11859-11867.
- Bilham, R., and B. Castillo (2020), The July 2019 Ridgecrest, California, Earthquake Sequence Recorded by Creepmeters: Negligible Epicentral Afterslip and Prolonged Triggered Slip at Teleseismic Distances, *Seismological Research Letters*, 91(2A), 707-720.
- Bonner, J. L., D. D. Blackwell, and E. T. Herrin (2003), Thermal Constraints on Earthquake Depths in California, *Bulletin of the Seismological Society of America*, 93(6), 2333-2354.
- Brandenberg, S. J., P. Wang, C. C. Nweke, K. Hudson, S. Mazzoni, Y. Bozorgnia, K. W. Hudnut, C. A. Davis, S. K. Ahdi, and F. Zareian (2019), Preliminary report on engineering and geological effects of the July 2019 Ridgecrest earthquake sequence *Rep.*, Geotechnical Extreme Event Reconnaissance Association.
- Chen, K., J. P. Avouac, S. Aati, C. Milliner, F. Zheng, and C. Shi (2020), Cascading and pulse-like ruptures during the 2019 Ridgecrest earthquakes in the Eastern California Shear Zone, *Nat Commun*, 11(1), 22.
- Feng, W., S. Samsonov, Q. Qiu, Y. Wang, P. Zhang, T. Li, and W. Zheng (2020), Orthogonal Fault Rupture and Rapid Postseismic Deformation Following 2019 Ridgecrest, California, Earthquake Sequence Revealed From Geodetic Observations, *Geophysical Research Letters*, 47(5).
- Ferrario, M. F., and F. Livio (2018), Characterizing the Distributed Faulting During the 30 October 2016, Central Italy Earthquake: A Reference for Fault Displacement Hazard Assessment, *Tectonics*, 37(5), 1256-1273.
- Fielding, E. J., Z. Liu, O. L. Stephenson, M. Zhong, C. Liang, A. Moore, S. H. Yun, and M. Simons (2020), Surface Deformation Related to the 2019 M w 7.1 and 6.4 Ridgecrest Earthquakes in California from GPS, SAR Interferometry, and SAR Pixel Offsets, *Seismological Research Letters*.
- Floyd, M., G. Funning, Y. Fialko, R. Terry, and T. Herring (2020), Survey and Continuous GNSS in the Vicinity of the July 2019 Ridgecrest Earthquakes, *Seismological Research Letters*.
- Goldberg, D. E., D. Melgar, V. J. Sahakian, A. M. Thomas, X. Xu, B. W. Crowell, and J. Geng (2020), Complex Rupture of an Immature Fault Zone: A Simultaneous Kinematic Model of the 2019 Ridgecrest, CA Earthquakes, *Geophysical Research Letters*, 47(3).
- Hartzell, S. H., and T. H. Heaton (1983), Inversion of strong ground motion and teleseismic waveform data for the fault rupture history of the 1979 Imperial Valley, California, earthquake, *Bulletin of the Seismological Society of America*, 73(6A), 1553-1583.
- Hudnut, K. W., L. Seeber, and J. Pacheco (1989), Cross-fault triggering in the November 1987 Superstition Hills earthquake sequence, southern California, *Geophysical Research Letters*, 16(2), 199-202.
- Kanamori, H., and D. Hadley (1975), Crustal structure and temporal velocity change in southern California, in *Earthquake Prediction and Rock Mechanics*, edited, pp. 257-280, Springer.
- Kikuchi, M., and H. Kanamori (1982), Inversion of complex body waves, *Bulletin of the Seismological Society of America*, 72(2), 491-506.
- Lapusta, N., and J. R. Rice (2003), Nucleation and early seismic propagation of small and large events in a crustal earthquake model, *Journal of Geophysical Research: Solid Earth*, 108(B4).

Li, S., G. Chen, T. Tao, P. He, K. Ding, R. Zou, J. Li, and Q. Wang (2020), The 2019 M w 6.4 and M w 7.1 Ridgecrest earthquake sequence in Eastern California: rupture on a conjugate fault structure revealed by GPS and InSAR measurements, *Geophysical Journal International*, 221(3), 1651-1666.

Lin, G. (2020), Waveform Cross-Correlation Relocation and Focal Mechanisms for the 2019 Ridgecrest Earthquake Sequence, *Seismological Research Letters*.

Liu, C., T. Lay, E. E. Brodsky, K. Dascher-Cousineau, and X. Xiong (2019), Coseismic Rupture Process of the Large 2019 Ridgecrest Earthquakes From Joint Inversion of Geodetic and Seismological Observations, *Geophysical Research Letters*, 46(21), 11820-11829.

Lomax, A. (2020), Absolute Location of 2019 Ridgecrest Seismicity Reveals a Shallow Mw 7.1 Hypocenter, Migrating and Pulsing Mw 7.1 Foreshocks, and Duplex Mw 6.4 Ruptures, *Bulletin of the Seismological Society of America*.

Lozos, J. C., and R. A. Harris (2020), Dynamic Rupture Simulations of the M 6.4 and M 7.1 July 2019 Ridgecrest, California, Earthquakes, *Geophysical Research Letters*, 47(7).

Mattioli, G. S., D. A. Phillips, K. M. Hodgkinson, C. Walls, D. J. Mencin, B. A. Bartel, D. J. Charlevoix, C. Crosby, M. J. Gottlieb, and B. Henderson (2020), The GAGE data and field response to the 2019 Ridgecrest earthquake sequence, *Seismological Research Letters*.

Melgar, D., T. I. Melbourne, B. W. Crowell, J. Geng, W. Szeliga, C. Scrivner, M. Santillan, and D. E. Goldberg (2019), Real-Time High-Rate GNSS Displacements: Performance Demonstration during the 2019 Ridgecrest, California, Earthquakes, *Seismological Research Letters*.

Meng, L., J.-P. Ampuero, J. Stock, Z. Duputel, Y. Luo, and V. C. Tsai (2012), Earthquake in a Maze: Compressional Rupture Branching During the 2012 M_w 8.6 Sumatra Earthquake, *Science*, 337(6095), 724-726.

Qiu, Q., S. Barbot, T. Wang, and S. Wei (2020), Slip Complementarity and Triggering between the Foreshock, Mainshock, and Afterslip of the 2019 Ridgecrest Rupture Sequence, *Bulletin of the Seismological Society of America*.

Renard, F., J. McBeck, and B. Cordonnier (2020), Competition between slow slip and damage on and off faults revealed in 4D synchrotron imaging experiments, *Tectonophysics*, 782-783, 228437.

Ross, Z. E., et al. (2019), Hierarchical interlocked orthogonal faulting in the 2019 Ridgecrest earthquake sequence, *Science*, 366(6463), 346-351.

Ruppert, N. A., C. Rollins, A. Zhang, L. Meng, S. G. Holtkamp, M. E. West, and J. T. Freymueller (2018), Complex faulting and triggered rupture during the 2018 MW 7.9 offshore Kodiak, Alaska, earthquake, *Geophysical Research Letters*, 45(15), 7533-7541.

Savage, J., W. Gan, and J. Svarc (2001), Strain accumulation and rotation in the Eastern California Shear Zone, *Journal of Geophysical Research: Solid Earth*, 106(B10), 21995-22007.

SCEDC (2013), Southern California Earthquake Data Center, *Caltech. Dataset*.

Scognamiglio, L., E. Tinti, E. Casarotti, S. Pucci, F. Villani, M. Cocco, F. Magnoni, A. Michelini, and D. Dreger (2018), Complex fault geometry and rupture dynamics of the MW 6.5, 30 October 2016, Central Italy earthquake, *Journal of Geophysical Research: Solid Earth*, 123(4), 2943-2964.

- Shelly, D. R. (2020), A High-Resolution Seismic Catalog for the Initial 2019 Ridgecrest Earthquake Sequence: Foreshocks, Aftershocks, and Faulting Complexity, *Seismological Research Letters*.
- Shi, Q., S. Wei, and M. Chen (2018), An MCMC multiple point sources inversion scheme and its application to the 2016 Kumamoto Mw 6.2 earthquake, *Geophysical Journal International*, 215(2), 737-752.
- Shi, Q., S. Barbot, S. Wei, P. Tapponnier, T. Matsuzawa, and B. Shibazaki (2020), Structural control and system-level behavior of the seismic cycle at the Nankai Trough, *Earth, Planets and Space*, 72(1), 27.
- Wang, K., and R. Bürgmann (2020), Co- and Early Postseismic Deformation Due to the 2019 Ridgecrest Earthquake Sequence Constrained by Sentinel-1 and COSMO-SkyMed SAR Data, *Seismological Research Letters*.
- Wang, X., and Z. Zhan (2020), Seismotectonics and fault geometries of the 2019 Ridgecrest sequence: insight from aftershock moment tensor catalog using 3D Green's functions, *Journal of Geophysical Research: Solid Earth*, e2020JB019577.
- Wei, S., D. Helmberger, and J. P. Avouac (2013a), Modeling the 2012 Wharton basin earthquakes off-Sumatra: Complete lithospheric failure, *Journal of Geophysical Research: Solid Earth*, 118(7), 3592-3609.
- Wei, S., D. Helmberger, Z. Zhan, and R. Graves (2013b), Rupture complexity of the Mw 8.3 sea of okhotsk earthquake: Rapid triggering of complementary earthquakes?, *Geophysical Research Letters*, 40(19), 5034-5039.
- Wei, S., M. Chen, X. Wang, R. Graves, E. Lindsey, T. Wang, Ç. Karakaş, and D. Helmberger (2018), The 2015 Gorkha (Nepal) earthquake sequence: I. Source modeling and deterministic 3D ground shaking, *Tectonophysics*, 722, 447-461.
- Wei, S., J.-P. Avouac, K. W. Hudnut, A. Donnellan, J. W. Parker, R. W. Graves, D. Helmberger, E. Fielding, Z. Liu, and F. Cappa (2015), The 2012 Brawley swarm triggered by injection-induced aseismic slip, *Earth and Planetary Science Letters*, 422, 115-125.
- Wessel, P., W. H. Smith, R. Scharroo, J. Luis, and F. Wobbe (2013), Generic mapping tools: improved version released, *Eos, Transactions American Geophysical Union*, 94(45), 409-410.
- Xu, S., and Y. Ben-Zion (2013), Numerical and theoretical analyses of in-plane dynamic rupture on a frictional interface and off-fault yielding patterns at different scales, *Geophysical Journal International*, 193(1), 304-320.
- Xu, X., D. T. Sandwell, and B. Smith-Konter (2020), Coseismic Displacements and Surface Fractures from Sentinel-1 InSAR: 2019 Ridgecrest Earthquakes, *Seismological Research Letters*.
- Yang, J., H. Zhu, and D. Lumley (2020), Time-lapse imaging of coseismic ruptures for the 2019 Ridgecrest earthquakes using multi-azimuth back-projection with regional seismic data and a 3D crustal velocity model, *Geophysical Research Letters*, e2020GL087181.
- Yoshida, S., K. Koketsu, B. Shibazaki, T. Sagiya, T. Kato, and Y. Yoshida (1996), Joint inversion of near-and far-field waveforms and geodetic data for the rupture process of the 1995 Kobe earthquake, *Journal of Physics of the Earth*, 44(5), 437-454.
- Zeng, H., S. Wei, and W. Wu (2020), Sources of uncertainties and artefacts in back-projection results, *Geophysical Journal International*, 220(2), 876-891.
- Zhang, Y., X. Zheng, Q. Chen, X. Liu, X. Huang, Y. Yang, Q. Xu, and J. Zhao (2020), Automatic inversion of rupture processes of the foreshock and mainshock and correlation of the seismicity during the 2019 Ridgecrest earthquake sequence, *Seismological Research Letters*, 91(3), 1556-1566.

507 Zhao, L.-S., and D. V. Helmberger (1994), Source estimation from broadband regional
508 seismograms, *Bulletin of the Seismological Society of America*, 84(1), 91-104.
509 Zhu, L., and D. V. Helmberger (1996), Advancement in source estimation techniques using
510 broadband regional seismograms, *Bulletin of the Seismological Society of America*, 86(5), 1634-
511 1641.
512 Zhu, L., and L. A. Rivera (2002), A note on the dynamic and static displacements from a point
513 source in multilayered media, *Geophysical Journal International*, 148(3), 619-627.
514